Journal of Alloys and Compounds 688 (2016) 329–335

Contents lists available at ScienceDirect

Journal of Alloys and Compounds

journal homepage: http://www.elsevier.com/locate/jalcom

Crystal structure and transporting properties of Bi_2S_3 under high pressure: Experimental and theoretical studies

Chunyu Li [a, 1], Jinggeng Zhao [b, 1], Qingyang Hu [a, c], Zhiguo Liu [d], Zhenhai Yu [a, *], Hao Yan [a, **]

[a] Center for High Pressure Science and Technology Advanced Research, Shanghai 201203, China
[b] Natural Science Research Center, Academy of Fundamental and Interdisciplinary Sciences, Harbin Institute of Technology, Harbin 150080, China
[c] Geophysical Laboratory, Carnegie Institution of Washington, Washington, DC 20015, USA
[d] Department of Physics, Harbin Institute of Technology, Harbin 150080, China

ARTICLE INFO

Article history:
Received 23 May 2016
Received in revised form
25 June 2016
Accepted 27 June 2016
Available online 29 June 2016

Keywords:
Pnictogen-chalcogen compounds
High pressure
Structural evolution
Electronic phase transition
Transporting properties

ABSTRACT

The high-pressure crystal structure and transporting properties of bismuthinite (Bi_2S_3) have been studied with a combination of experimental and theoretical methods. The present experimental results show that the structure of orthorhombic Bi_2S_3 stably exists in the experimental pressure range up to around 55 GPa. Upon compression, the X-Ray diffraction (XRD) patterns are dominated by broad Bragg features and seemingly pressure-induced structural amorphization or disorder occurs. However, by analyzing the XRD data obtained during the decompression cycle we suggest that the broad Bragg diffraction peaks under high pressure could be due to the nonhydrostatic conditions or crystal structural defects. To construct the correlation between the structural variation and the physical properties of Bi_2S_3, the transporting properties of Bi_2S_3 were investigated under high pressure. With increasing pressure, the resistance value decreases sharply below 5 GPa and then decreases gently as the pressure further increasing. There is an obvious inflection point at about 5 GPa in the relationships of log (R) versus pressure. We speculate that the observed electrical variation is resulted from the pressure-induced second-order isostructural phase transition according to the reported literature. Temperature dependence of the resistance indicated that a pressure-induced semiconductor → metal transition in Bi_2S_3 happens at around 20 GPa. The present high pressure resistance measurement indicated that high pressure could help to improve the thermoelectric properties.

1. Introduction

The pnictogen–chalcogen binary compounds with common formula V_2VI_3 (V = As, Sb, Bi; VI = S, Se, Te) usually show excellent photocatalytic activity [1,2]. Among these compounds, Bi_2S_3 is a typical prototype with direct gap band energy of 1.3–1.7 eV [3–6] and could be applied in thermoelectric [7], electronic [8], and optoelectronic devices [9]. The crystal structure of bismuth sulfide Bi_2S_3 occurs naturally in the form of orthorhombic bismuthinite. Bi_2S_3 as well as its sister compound Sb_2S_3 has attracted much attention due to their lone electron pairs (LEP) on cations [10]. The crystal structure of Bi_2S_3 was refined by Kyono et al. by single crystal diffraction method [11]. Orthorhombic Bi_2S_3 is a strongly anisotropic structure with space group *Pnma* that contains 20 atoms (4 chemical formulas) per unit cell. Each Bi^{3+} ions are in a highly distorted octahedral geometry. The discovery of topological insulators (TIs) in V_2VI_3-type compounds Bi_2Se_3 and Bi_2Te_3 opened a new era in fundamental topological physics, and attracted much attention in experimental and theoretical investigations [12,13]. Bi_2Se_3 and Bi_2Te_3 have various actual applications, such as thermoelectric materials, besides the comprehensive theoretical investigations in condensed matter physics. Both Bi_2Te_3 and Bi_2Se_3 compounds adopt a rhombohedral structure (R-3m, Z = 3) at ambient conditions, which is made up of Se(Te)-Bi-Se(Te)-Bi-Se(Te) quintuple layers piled up along the c-axis. Bi_2Se_3 and Bi_2Te_3 can be seen as substituting S in Bi_2S_3 with the same VI main group elements Se and Te, while the structure of them falls into a completely different class from Bi_2S_3.

Pressure, together with temperature, is a key external variable which can tune structures and corresponding properties of materials. In addition to the remarkable effect on the crystal structures of

* Corresponding author.
** Corresponding author.
E-mail addresses: yuzh@hpstar.ac.cn (Z. Yu), yanhao@hpstar.ac.cn (H. Yan).
[1] These authors contributed equally to this study and share first authorship.

http://dx.doi.org/10.1016/j.jallcom.2016.06.276
0925-8388/

Bi_2Se_3, previous studies have also shown that pressure could significantly affected the transporting properties such as pressure-induced superconductivity at ~11 GPa in Bi_2Se_3 [14]. The hydrostatic pressure effects on the electronic, optical, and photocatalytic properties of ribbon-like Bi_2S_3 have been investigated by E. Zahedi [15] using density functional theory (DFT) calculations. The theoretical results indicated that the photocatalytic activity of the ribbon-like Bi_2S_3 decreases with increasing hydrostatic pressure. The high-pressure crystal structure and the cation LEP activity of Bi_2S_3 were investigated by L. F. Lundegaard et al. up to 10 GPa [10]. The experimental results have shown that the crystal structure of Bi_2S_3 is stable during the covered pressure range. However, Efthimiopoulos et al. [16] observed notable changes of the axial ratios for the *Pnma* phase Bi_2S_3 around 4–6 GPa by detailed structural and Raman spectroscopic results, and claimed that a second-order isostructural transition occurs in the *Pnma* phase Bi_2S_3.

Pressure could suppress the lone electron pair of Bi_2S_3, which may result in the structural phase transition and the change of electronic properties. Although there are many reports on the structural evolutions of Bi_2S_3, scarce information is known about its high-pressure transporting behavior by now. Therefore, in this work, we report detailed experimental and theoretical studies on the structural and transporting properties of Bi_2S_3 under pressure up to 55 and 25.6 GPa, respectively.

2. Experimental and theoretical methods

2.1. High-pressure synchrotron angle dispersive XRD

In this work, Bi_2S_3 sample was purchased from Alfa Aesar's company with 99.9% purity. The high-pressure synchrotron XRD experiment was carried out at room temperature using a symmetric diamond anvil cell (DAC) with 300 μm. T301 stainless steel was served as the gasket. A 100 μm gasket hole was made by drilling at the center of indention in the foil. The sample chamber was filled with a mixture of Bi_2S_3 powder, a ruby chip, and silicone oil as the pressure-transmitting medium. Angle dispersive XRD (AD-XRD) patterns were obtained with a MarCCD detector at the X17C beamline of the National Synchrotron Light Source (NSLS), Brookhaven National Laboratory (BNL), and the BL15U1 beamline of the Shanghai Synchrotron Radiation Source (SSRF) using monochromatic radiation with a wavelength of 0.4112 and 0.6199 Å, respectively. The sample to detector distance for X17C and BL15U1 was 288.3593 and 175.8369 mm, respectively. The Fit2D software package was used to process the data [17]. The pressures were determined according to the fluorescence shift of ruby [18]. The XRD patterns of Bi_2S_3 were analyzed with Rietveld refinement using the GSAS program package [19] with a user interface of EXPGUI [20].

2.2. High-pressure electrical transport properties measurement

A symmetric DAC with a diamond culet size of 400 μm was used to apply the pressure. The high-pressure electrical resistance measurement for Bi_2S_3 was performed using a four-electrode method without pressure transmitting medium. The pressures were determined according to the fluorescence shift of ruby [18]. Four electrodes were set up on one side of the diamond anvil. And a T301 stainless steel gasket was put on the other side, in which a smaller hole of 150 μm in diameter was drilled to serve as the sample chamber. To build insulation to the electrodes, the hole in the gasket was filled by the compacted c-BN powder and the rest part of the gasket was covered by the insulating gel. The resistance measuring DAC was checked by ohmmeter to make sure that it works well before taking measurement. To implicitly observe the different temperature effects on semiconductor and metal, the high-temperature and high-pressure resistance measurement for Bi_2S_3 was also conducted.

2.3. First-principle calculations

The calculations were performed in the framework of density functional theory (DFT) through Vienna *ab initio* simulation package [21]. The Generalized gradient approximation (GGA) under Perdew-Burke-Ernzerhof parametrization [22] was implemented to describe the exchange correlation functionals. We used normal valence electrons configurations for S atoms ($3s^2 3p^4$) and included semicore electrons for Bi atoms ($5d^{10} 6s^2 6p^3$). A plane-wave basis set with 500 eV kinetic energy cut off was employed to converge energy and optimize geometry of Bi_2S_3 until force acting on each atom is less than 0.01 eV $Å^{-1}$. The Brillouin zone was sampled by a Monkhorst mesh of $8 \times 4 \times 8$ k points using tetrahedron integration scheme. Our calculation incorporated spin-orbit coupling effects and non-collinear magnetic calculation. Those relativistic corrections are found not negligible in metal chalcogenides like Bi_2S_3 and Bi_2Se_3 [4]. Pressure was applied by adding pulay stress to the diagonal elements of the stress tensor. The crystal band structures were recalculated from the optimized charge density with sets of *k*-points along the high-symmetry points in the Brillouin zone.

3. Results and discussion

3.1. High pressure angle dispersive XRD patterns of Bi_2S_3

In order to clarify potential structural changes at high pressure, the *in situ* high pressure powder AD-XRD experiment for Bi_2S_3 was carried out at room temperature with a stepwise pressure increasing up to 30.8 GPa as shown in Fig. 1(a). At ambient conditions, we found Bi_2S_3 crystallizes into an orthorhombic structure (space group: *Pnma*). As the pressure gradually increases, the diffraction peaks for the *Pnma* phase of Bi_2S_3 shift steadily to higher angle, indicating the shrinking of lattices. Apart from the peak shift, the diffraction peaks become broader and the intensity of the AD-XRD patterns decreases above 22.0 GPa and no new diffraction peaks emerges up to 30.8 GPa (Run 1) and 55.0 GPa (Run 2, Fig. 1(b)). The feature of AD-XRD patterns of Bi_2S_3 under high pressure was speculated undergoing a pressure-induced amorphization or disorder according to the reported literature [16]. Furthermore, as a sister compound to Bi_2S_3, a pressure-induced amorphization in α-Bi_2O_3 was discovered by Pereira et al. between 15 and 25 GPa [23]. However, the broadening and weakening of diffraction patterns suffered from several factors such as (i) grain size effects; (ii) the quasihydrostatic/nonhydrostatic pressure environment; (iii) strong crystallographic distortion; (iV) structural disorder defects or disorder/amorphization. To address the above mentioned issues, we have also taken AD-XRD patterns during the decompression cycle as shown in Fig. 1(b). The diffraction peaks could be still indexed by the ambient orthorhombic phase after the pressure was released to 1.8 GPa as shown in Fig. 1(c), indicating that the orthorhombic *Pnma* phase of Bi_2S_3 shows the tendency of disorder under high pressure (55.0 GPa) and could not fully recover to parent phase after decompression from high pressure (compression to 55.0 GPa). The *Pnma* phase could stably exist in our experimental pressure range. The experimental results obtained at BL15U1 beamline at SSRF, as shown in Fig. S1 (see Supplemental Material for details) [24], are consistent with those collected at X17C beamline at BNL.

The high-pressure XRD patterns of the *Pnma* phase Bi_2S_3 can be obtained by the Rietveld refinement. The refinement result at

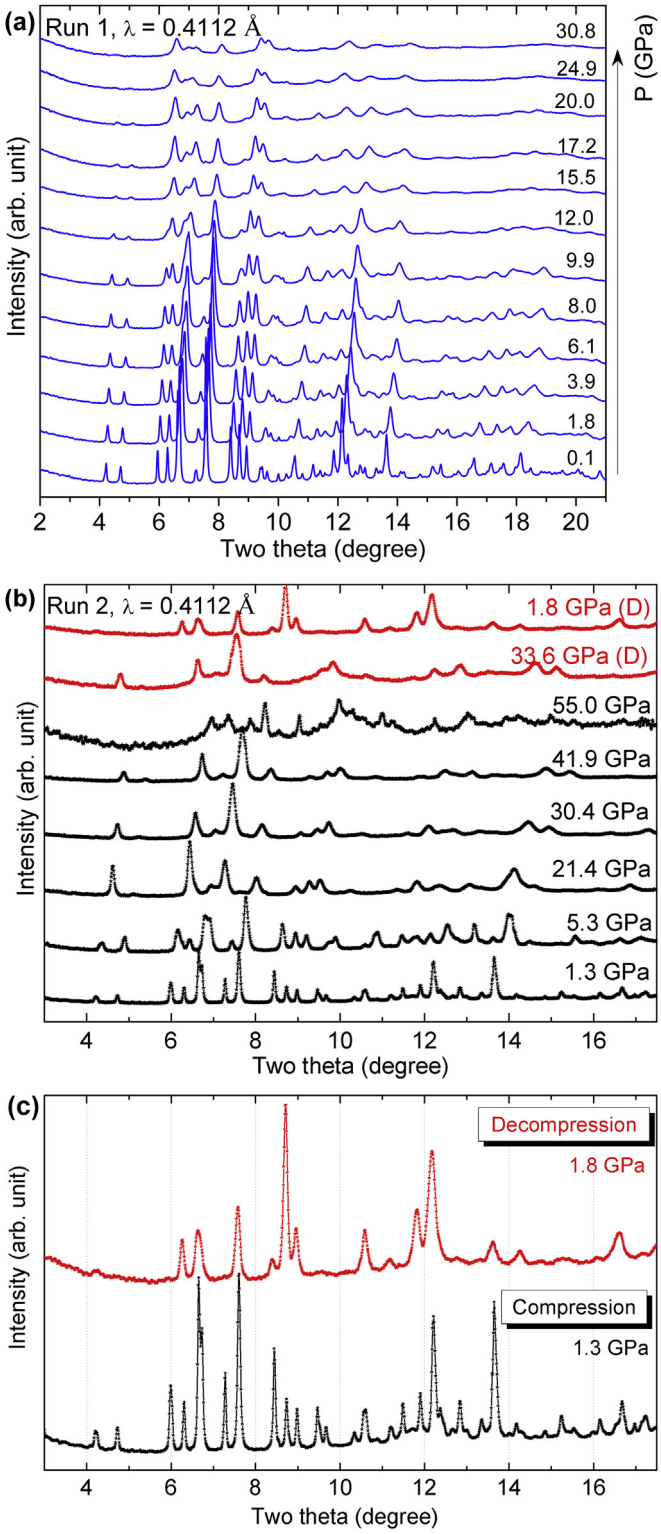

Fig. 1. (a) Selected AD-XRD patterns of Bi_2S_3 measured at room temperature and different pressures (Run 1, up to 30.8 GPa). (b) Run 2 up to 55.0 GPa, the top pattern corresponds to XRD patterns collected during decompression from 55.0 GPa. (c) The comparison of XRD patterns taken in compression (1.3 GPa) and decompression (1.8 GPa) cycles.

0.6 GPa is shown in Fig. 2. The vertical bars represent the calculated positions of the diffraction peaks of Bi_2S_3. The difference between the observed (circles) and the fitted patterns (line) is shown with a dotted green line at the bottom of the diffraction peaks.

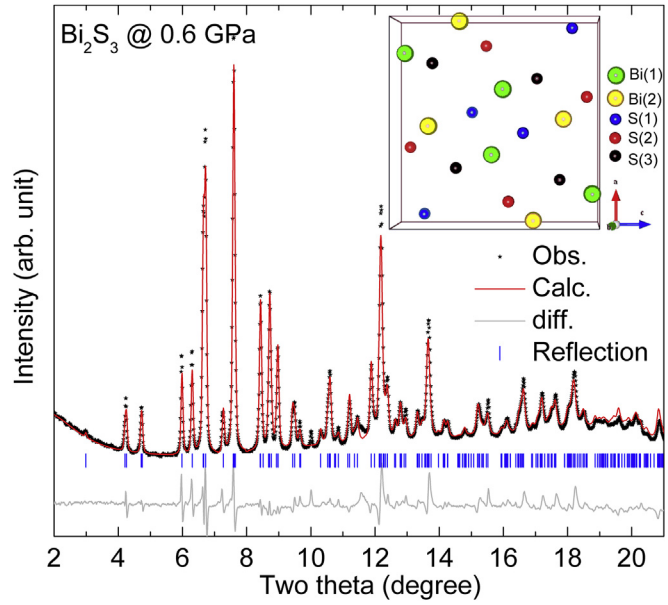

Fig. 2. Typical Rietveld refinement of *Pnma* phase of Bi_2S_3 at 0.6 GPa (λ = 0.4112 Å). The vertical bars represent the calculated positions of the diffraction peaks of Bi_2S_3. The difference between the observed (circles) and the fitted patterns (line) is shown with a dotted green line at the bottom of the diffraction peaks. (For interpretation of the references to colour in this figure legend, the reader is referred to the web version of this article.)

The lattice parameters for the *Pnma* phase of Bi_2S_3 are obtained from the refined XRD patterns, which homogeneously decrease as the pressure increases. To deeply investigate the crystal structure variation, the pressure dependences of the lattice parameters ratios (a/b, a/c and c/b) for Bi_2S_3 are shown in Fig. 3. It is interesting to note that the axial ratio (a/c) show an inflection point around 3 GPa. This pressure-induced turning point may give rise to the variation of transporting properties (see transporting properties section). Lundegaard et al. investigated the pressure effect on the LEP of Sb_2S_3

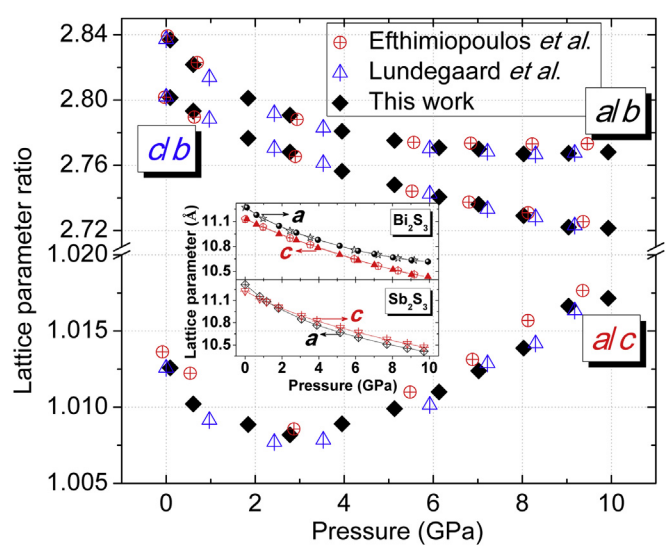

Fig. 3. The pressure evolution of the lattice parameter ratios for the *Pnma* phase Bi_2S_3 (including the present and the literature data). The inset shows the pressure dependences of the lattice parameters (a and c) of Bi_2S_3 (this work (solid symbol) and Ref. [10] (open symbol)) and Sb_2S_3 (Ref. [25] (open symbol)).

and Bi_2S_3 at ambient and high-pressure conditions by DFT calculations [10]. It was found that the LEP is mainly located along *a*-axis at ambient pressure and the configuration of LEP becomes much more symmetric at high pressure. The present high-pressure axial ratio results are consistent with the configurations of LEP in Sb_2S_3 and Bi_2S_3 [10]. The pressure dependences of the lattice parameters (*a* and *c*) for the *Pnma* phase of Bi_2S_3 and Sb_2S_3 are shown in the inset of Fig. 3, which decrease as the increasing pressure for both Bi_2S_3 and Sb_2S_3 [10,25]. While the lattice parameters *a* and *c* exhibit cross at around 1.12 GPa for Sb_2S_3. The slightly longer zero-pressure length and higher compressibility of the *a*-axis compared to the *c*-axis result in this crossing. However, the lattice parameters *a* and *c* in Bi_2S_3 doesn't show the similar crossing in the pressure range of 0–10 GPa. The above results are also related to the configurations of LEP in Sb_2S_3 and Bi_2S_3. The effective ionic radii of the trivalent ions Sb^{3+}, Bi^{3+} are 0.76 and 1.03 Å, respectively [26]. Therefore, the LEP phenomenon in Bi_2S_3 is not as obvious as in Sb_2S_3. This is in agreement with the DFT simulation results from Ref. [10].

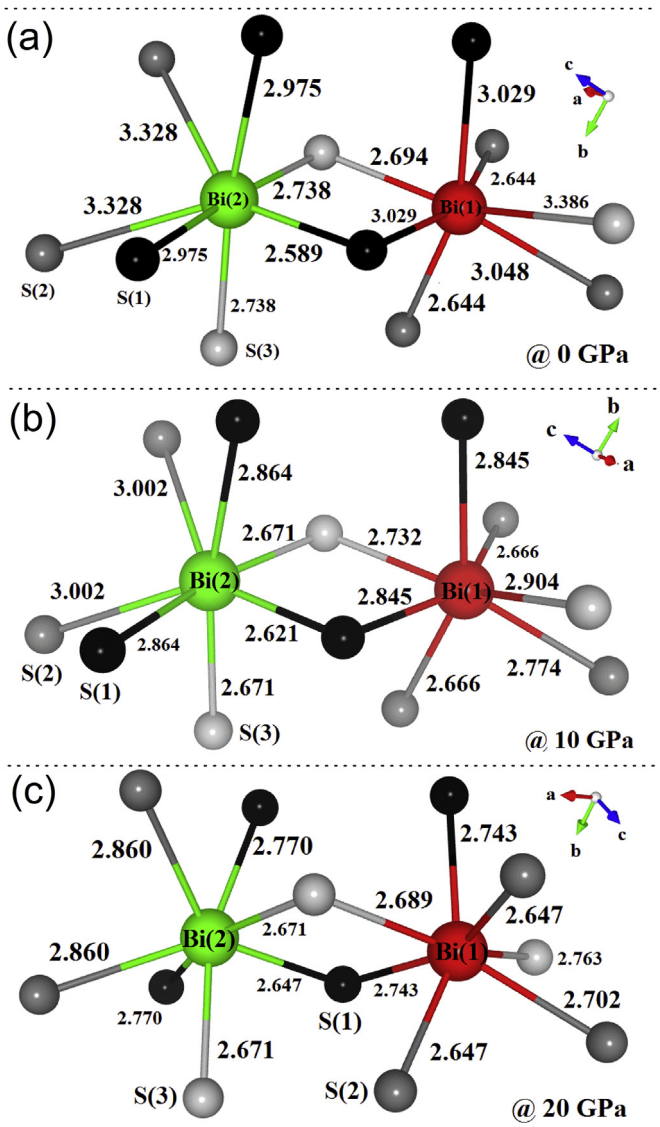

Fig. 4. The bonding lengths of Bi_2S_3 under several selected pressures ((a) 0 GPa, (b) 10 GPa and (c) 20 GPa). The numbers represent the corresponding Bi-S distances (in Å). The bonding length between two ribbons was strongly compressed as the pressure increasing. However, the bonding lengths in the ribbons possess minor variation under high pressure.

The bonding lengths in Bi_2S_3 under several selected pressure points are shown in Fig. 4. The bonding lengths at 0 and 10 GPa are derived from the present lattice constants. The atomic positions were gained from Ref. [10]. The bonding length at 20 GPa is obtained from the present experimental and DFT simulations. There are two distinct Bi positions in the *Pnma* phase Bi_2S_3. Each Bi atom is coordinated to seven S atoms and bonded to three S atoms with short bonding distances of 2.589–2.738 Å and four S atoms with longer distances of 2.975–3.328 Å at 0 GPa. Because the covalent radius for S and Bi atoms is 1.05 and 1.48 Å at ambient conditions, respectively [27], these short-bonded Bi and S build strongly bonded ribbons perpendicular to the *b*-axis. The Van der Waals radius for Bi and S is 2.1 and 1.8 Å, respectively. Just the Van der Waals force exists between the longer-bonded Bi and S atoms. Therefore, there are only weak interactions between the adjacent ribbons along the *b*-axis (Fig. 4(a)). It can be seen from Fig. 4(b) and (c) that the four longer Bi-S bondings exhibited strong shrink as the increasing pressure. The longest Bi-S bonding shows 14% shrink up to 20 GPa. However, the three shorter Bi-S bondings did not exhibit remarkable variation as the increasing pressure. This is consistent with the chemical bonding results that Bi and S are covalently bonded in the Bi_4S_6 ribbons. The number of short Bi-S bonding increases from 3 (0 GPa) to 5 (20 GPa) according to the present and literature results. This will affect the transporting behavior of Bi_2S_3 under high pressure (see the subsequent transporting study section).

Table 1 summarized the bulk modulii and the corresponding pressure derivatives for V_2VI_3-type compounds from literature and the present work. The bulk modulus of Bi_2S_3 can be compared with other V_2VI_3-type compounds. The bulk modulii for the group V elements (As, Sb, and Bi) and the group VI elements (S, Se, and Te) are 22, 42, 31, and 7.7, 8.3, 65 GPa, respectively [28]. From these elemental bulk modulii, it can be seen that the V_2VI_3-type compounds possess similar bulk modulii to their elements due to the weak Van der Waals bonding between ribbons. Table 1 shows that the value of bulk modulus for one compound is different from different research groups. As has been already observed in other materials, the use of different pressure media (which may produce different deviatoric stresses) could affect the pressure dependence of the unit-cell volume, thus influencing the determination of the values of B_0 and its pressure derivative B_0' that has a strong correlation with the bulk modulus. Besides, it is noteworthy that using different orders (2nd or 3rd) of EOS also affect the fitting values of the bulk modulii and the lattice volumes at ambient pressure [29].

3.2. Transporting behavior of Bi_2S_3 under high pressure

We now turn to the investigation on the transporting properties

Table 1
The selected zero-pressure bulk modulus (B_0), and its pressure derivative (B_0') for the typical V_2VI_3-type compounds by fitting Birch-Murnaghan's equation of state (BM-EOS). Experimental and theoretical values reported in the literature are provided for comparison.

	Type of EOS	Order of EOS	B_0 (GPa)	B_0'	Reference
Sb_2S_3	BM-EOS	3rd	26.91 (14)	7.9 (1)	[25]
	BM-EOS	2nd	27.2 (6)	6.0	[30]
Sb_2Se_3	BM-EOS	3rd	30 (1)	6.1 (0.2)	[31]
Sb_2Te_3	BM-EOS	2nd	45 (2)	4.0	[32]
		2nd	54.7	4.0	[33]
Bi_2S_3	BM-EOS	3rd	36.6 (15)	6.4 (5)	[10]
		3rd	38.9 (8)	5.5 (1)	[16]
		3rd	37.5 (3)	4.6	This work
Bi_2Se_3	BM-EOS	2nd	53.1 (7)	4.0	[34,35]
		3rd	53 (8)	2.9 (2)	[36]
Bi_2Te_3	BM-EOS	3rd	36.3 (1)	5.5 (1)	[37]
		3rd	38.19 (0.42)	4.61 (0.16)	[38]

of Bi_2S_3 under high pressure. A structural or iso-structural phase transition is often accompanied by an electronic phase transition. The distance deceasing of the atoms in the intra-as well as interlayers of Bi_2S_3 is expected to modulate the electronic properties, which can be reflected by the electronic transport property measurement. At ambient pressure, Bi_2S_3 is a semiconductor with band gap of 1.3–1.7 eV [3–6]. The resistance–pressure relation measured for Bi_2S_3 is plotted in Fig. 5. It can be seen that the resistance appears a steep decrease of about three orders of magnitude during the pressure range of 0–12 GPa Bi_2S_3 has recently attracted more and more interests for its potential application in thermoelectric field due to its high Seebeck coefficient and low thermal conductivity at room temperature. However, the high electrical resistivity is still the main reason for its low thermoelectric property at present [39,40]. The present high pressure resistance measurement indicated that high pressure could help to improve the thermoelectric properties of Bi_2S_3. The previous investigation showed that the electrical resistivity of Bi_2S_3 could be reduced by 2–3 orders of magnitude through introducing sulfur vacancies in the lattice [41]. It is interesting to note that this phenomenon is similar with the resistivity changing of Bi_2S_3 under high pressure in our present work. We know that the coordination number (CN) of Bi increased from 3 to 5 as the pressure increasing from our chemical bonding studies. The resistance decrease of Bi_2S_3 and the CN increase of Bi indicate that more electrons will participate into the conduction process as the pressure increasing and result in the enhancement of the density of charge carrier.

To discern the novel change of the electrical resistance more clearly, the corresponding log(R)–P relations are plotted in the inset (top left) of Fig. 5. The log(R)–P curve shows an inclination around the pressure of 5 GPa. Finally, the resistance almost saturate to their minimum values up to around 25.7 GPa. The inclination in the log(R)–P curve around 5 GPa is claimed to correlate with the variation of the crystal structure of Bi_2S_3 [16]. To determine whether or not Bi_2S_3 undergoes a semiconductor–metal transformation under high pressure, the temperature dependence of the resistance was also measured for Bi_2S_3 at several representative pressures (shown in the bottom right inset of Fig. 5). It can be seen that the temperature coefficients of Bi_2S_3 are negative ($dR/dT < 0$) below the pressure of 18.0 GPa, indicating that Bi_2S_3 has the semiconductor behavior, and the absolute value of dR/dT decreases as the pressure increasing up to 18.0 GPa. It is remarkable to note that the resistance of Bi_2S_3 starts to increase as the temperature further increasing; that is, the temperature coefficients of Bi_2S_3 become positive ($dR/dT > 0$) above 20.9 GPa, indicating that Bi_2S_3 has a semiconductor-metal electronic phase transition above this pressure point. While it is interesting to note that there is no noticeable anomalous variation for the log(R)–P curve around 20.9 GPa. We attribute this to the pressure-induced semiconductor-metal transition in Bi_2S_3 resulted from the step-by-step merge of the electronic band gap. This speculation was confirmed by the following DFT calculation results of the band structures (see section 3.3). However, the anomalous variation of the electrical resistance around 5 GPa is due to the second-order isostructural phase transition, at which pressure point Bi_2S_3 is still a semiconductor.

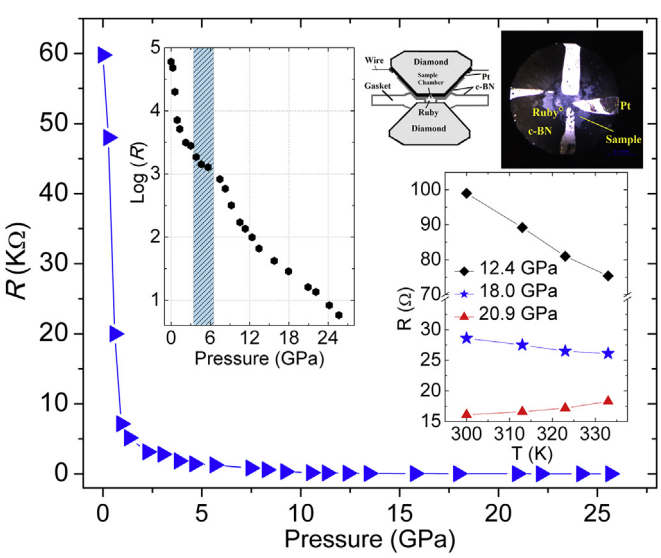

Fig. 5. Pressure dependence of the electrical resistances for Bi_2S_3. The upper-left inset shows the pressure dependence of the log(R). Upper-right corner inset shows the schematic diagram of the experimental setup for high pressure resistance measurements (side view) and experimental setup image of electrical measurement under high pressure (vertical view). The bottom-right inset shows the temperature dependence of electrical resistance in Bi_2S_3 under various pressures up to 25.7 GPa. The pressure-induced semiconductor→metal transition around 20.9 GPa is characterised by contrasting the temperature dependence of resistance under different pressures.

3.3. Theoretical simulation Bi_2S_3 under high pressure

As mentioned above, the high-pressure electrical resistance measurement observed a pressure-induced semiconductor→metal transition in Bi_2S_3 around 20.9 GPa without detectable crystallographic variation from the AD-XRD. It was just suggested as a pressure-induced electronic phase transition. To address the foregoing issues, the high-pressure electronic property of Bi_2S_3 was investigated using DFT simulations. The present calculated ground-state lattice parameters and band gap agree reasonably with the former experimental results [10], indicating the rationality of our selected pseudopotential and exchange-correlation function.

The electronic structure of Bi_2S_3 was evaluated by first-principles calculations. Fig. 6 shows the energy band structure of Bi_2S_3 along the principal high-symmetry directions in the Brillouin zone under 0 and 33 GPa. The ambient *Pnma* phase processes an indirect band gap of 1.19 eV (Fig. 6(a)). Here the value of the energy band gap is defined as the difference between the conduction band minimum (CBM) and the valence band maximum (VBM). The calculated band gap value (1.19 eV) at ambient pressure is agreement with the experimental value of 1.30–1.70 eV [3–6]. It predicts that the *Pnma* phase Bi_2S_3 at ambient pressure is a semiconductor with an indirect band gap, which is consistent with Zahedi's calculation results [15]. The band gap of Bi_2S_3 decreases as the pressure increasing and Bi_2S_3 will be more appropriate for the absorption of sun light when the decreased band gap reach at ~0.9 eV [42]. As the pressure further increasing, the valence band and conduction band merge together at 33.0 GPa (Fig. 6(b)), indicating Bi_2S_3 transforms into metallic state. Since the calculated band structure is very sensitive to the size of crystal lattice [4], the higher metallization pressure predicted from simulation is most likely a result of thermodynamics effects.

Table 2 summarizes the crystallographic symmetry, band gap at ambient conditions and electronic phase transition pressure for different V_2VI_3-type compounds reported in the literature and present work. From Table 2, it can be seen that the band gap decreases as the atomic number increasing and the merge of energy band demanding higher pressure for lighter V_2VI_3-type semiconductor. For the V_2VI_3-type tellurides, it should be mentioned that the crystallographic environment of the $C2/m$ (six-fold) phase As_2Te_3 at ambient pressure is different from the high-pressure $C2/m$ (seven-fold) phase Bi_2Te_3 and Sb_2Te_3. Our recent high-pressure electrical measurement and theoretical simulation showed that As_2Te_3 undergoes a pressure-induced insulator–semimetal–metal transition [43]. Sb_2Te_3 possess the same crystallographic symmetry

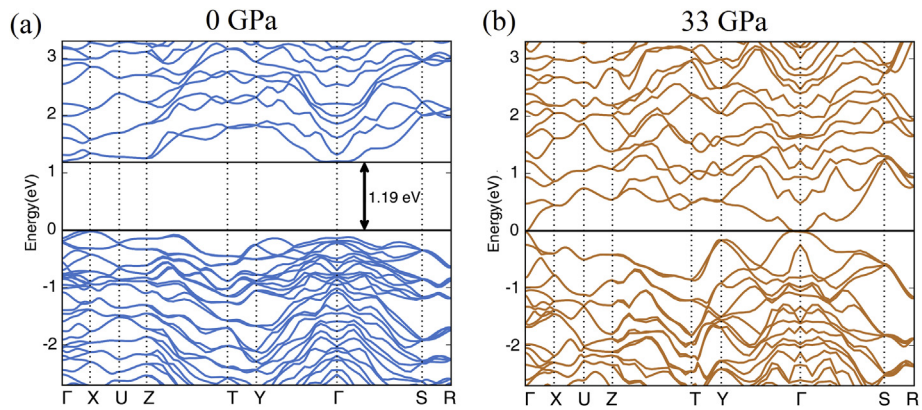

Fig. 6. The calculated band structures of Bi_2S_3 under selected pressures. (a), 0 GPa, (b) 33 GPa. The Fermi energy (E_F) is set to be 0 eV. The band gap merged around 33 GPa.

Table 2
The crystallographic symmetry, band gap at ambient conditions and the electronic phase transition pressures for different V_2VI_3-type compounds. SC and M denote semiconductor and metal, respectively.

	Space group	Eg (eV)	SC → M (GPa)	Reference
As_2S_3	$P2_1/c$	2.7[a]	45.0	[44]
As_2Se_3	$P2_1/c$	1.7[a]	21.0	[45]
As_2Te_3	$C2/m$	0.8[a]	14.9	[43]
Sb_2S_3	*Pnma*	1.7–1.8[b]		[46]
Sb_2Se_3	*Pnma*	1.00[b]	3.0	[47]
Sb_2Te_3	*R*-3*m*	0.28[b]	9.5	[48]
Bi_2S_3	*Pnma*	1.30[b]	20.9	[This work]
Bi_2Se_3	*R*-3*m*	0.30[b]	9.7	[14]
Bi_2Te_3	*R*-3*m*	0.12[b]	9.2	[49]

[a] The value of band gap was referenced from Ref. [45] and reference therein.
[b] The value of band gap was referenced from Ref. [46] and reference therein.

(*R*-3*m*) as that of Bi_2Se_3 and Bi_2Te_3 at ambient conditions. Both Bi_2Se_3 and Bi_2Te_3 showed pressure-induced semiconductor → metal transition around 9 GPa. However, the isocompounds Sb_2Te_3 did not follow the same pressure-induced semiconductor → metal transition.

4. Conclusions

To summarize, we have investigated the structural stability of Bi_2S_3 up to 55 GPa through the *in situ* high pressure AD-XRD experiments. The ambient-pressure *Pnma* phase is stable in the present studied pressure range. The diffraction peaks broadening under high pressure (>30 GPa) is not resulted from pressure-induced amorphization/disorder by the present experimental analysis. The electric resistance measurement shows that resistance decreases by three magnitudes around the pressure of 5 GPa, which is caused by the second-order phase transition. The high-temperature and high-pressure electrical resistance measurement indicated that Bi_2S_3 experiences a semiconductor-to-metal transition around 20.9 GPa. And our energy band structure calculation results agree well with above experimental results. The thermoelectric development of Bi_2S_3 is hindered from its high electrical resistivity. It is quite encouraging that the electrical resistivity of Bi_2S_3 under high pressure could improve its thermoelectric properties.

Acknowledgements

We acknowledge the National Synchrotron Light Source (NSLS) of Brookhaven National Laboratory (BNL) for the provision of synchrotron radiation facilities beam line X17C. Use of NSLS is supported by the U.S. Department of Energy (DOE), Office of Science, Office of Basic Energy Sciences, under Contract DEAC02-98CH10886. We are thankful for the support from COMPRES (the Consortium for Materials Properties Research in Earth Sciences). Portions of this work were performed at the BL15U1 beamline, shanghai synchrotron radiation facility in China. The authors would like to thank Shanghai Synchrotron Radiation Source for use of the synchrotron radiation facilities. This work was partially supported by Natural Science Foundation of China (Grant No. 11274081 and 10904022). The computational work was conducted on the SR10000-K1/52 supercomputing facilities of the Institute for Materials Research, Tohoku University. We are grateful to the editor and anonymous referees for their thorough reading of the paper and suggestion for improvement.

Appendix A. Supplementary data

Supplementary data related to this article can be found at http://dx.doi.org/10.1016/j.jallcom.2016.06.276.

References

[1] F.J. Chen, Y.L. Cao, D.Z. Jia, J. Colloid Interface Sci. 404 (2013) 110.
[2] E.L. Hu, X.H. Gao, A. Etogo, Y.L. Xie, Y.J. Zhong, Y. Hu, J. Alloy Compd. 611 (2014) 335.
[3] J. Black, E.M. Conwell, L. Seigle, C.W. Spencer, J. Phys. Chem. Solids 2 (1957) 240.
[4] M.R. Filip, C.E. Patrick, F. Giustino, Phys. Rev. B 87 (2013) 205125.
[5] V. Stavila, K.H. Whitmire, I. Rusakova, Chem. Mater. 21 (2009) 5456.
[6] Y. Sharma, P. Srivastava, A. Dashora, L. Vadkhiya, M.K. Bhayani, R. Jain, A.R. Jani, B.L. Ahuja, Solid State Sci. 14 (2012) 241.
[7] X.L. Du, F.S. Cai, X.W. Wang, J. Alloys Compd. 587 (2014) 6.
[8] X.H. Huang, Y.W. Yang, X.C. Dou, Y.G. Zhu, G.H. Li, J. Alloys Compd. 461 (2008) 427.
[9] Y. Wang, J.Y. Chen, L.X. Jiang, K.L. Sun, F.Y. Liu, Y.Q. Lai, J. Alloys Compd. 686 (2016) 684.
[10] L.F. Lundegaard, E. Makovicky, T. Boffa-Ballaran, T. Balic-Zunic, Phys. Chem. Min. 32 (2005) 578.
[11] A. Kyono, M. Kimata, Am. Mineral. 89 (2004) 932.
[12] Y.L. Chen, J.G. Analytis, J.-H. Chu, Z.K. Liu, S.-K. Mo, X.L. Qi, H.J. Zhang, D.H. Lu, X. Dai, Z. Fang, S.C. Zhang, I.R. Fisher, Z. Hussain, Z.-X. Shen, Science 325 (2009) 178.
[13] H.J. Zhang, C.X. Liu, X.L. Qi, X. Dai, Z. Fang, S.C. Zhang, Nat. Phys. 5 (2009) 438.
[14] K. Kirshenbaum, P.S. Syers, A.P. Hope, N.P. Butch, J.R. Jeffries, S.T. Weir, J.J. Hamlin, M.B. Maple, Y.K. Vohra, J. Paglione, Phys. Rev. Lett. 111 (2013) 087001.
[15] E. Zahedi, Superlattice Microst 81 (2015) 49.
[16] I. Efthimiopoulos, J. Kemichick, X. Zhou, S.V. Khare, D. Ikuta, Y.J. Wang, J. Phys. Chem. A 118 (2014) 1713.
[17] A.P. Hammersley, S.O. Svensson, M. Hanfland, A.N. Fitch, D. Hausermann, High. Press. Res. 14 (1996) 235.
[18] H.K. Mao, J. Xu, P. Bell, J. Geophys. Res. 91 (1986) 4673.
[19] A.C. Larson, R.B. Von Dreele, General Structure Analysis System, GSAS, Los

Alamos National Laboratory Report LAUR 86-748, 1994.
[20] B.H. Toby, J. Appl. Crystallogr. 34 (2001) 210.
[21] G. Kresse, J. Hafner, Phys. Rev. B 49 (1994) 14251.
[22] J.P. Perdew, K. Burke, M. Ernzerhof, Phys. Rev. Lett. 77 (1996) 3865.
[23] A.L.J. Pereira, D. Errandonea, A. Beltran, L. Gracia, O. Gomis, J.A. Sans, B. Garcıa-Domene, A. Miquel-Veyrat, F.J. Manjon, A. Munoz, C. Popescu, J. Phys. Condens. Matter. 25 (2013) 475402.
[24] See supplementary material at http://dx.doi.org/10.1016/j.jallcom.2016.06.276 for detailed HP-XRD of Bi2S3 at BL15U1 of SSRF.
[25] L.F. Lundegaard, R. Miletich, T. Balic-Zunic, E. Makovicky, Phys. Chem. Miner. 30 (2003) 463.
[26] R.D. Shannon, Acta Crystallogr. A 32 (1976) 751.
[27] B. Cordero, V. Gómez, A.E. Platero-Prats, M. Revés, J. Echeverría, E. Cremades, F. Barragán, S. Alvarez, Dalton Trans. 21 (2008) 2832.
[28] K. Gschneidner Jr., Solid State Phys. 16 (1964) 275.
[29] R.J. Angel, J.L. Mosenfelder, C.S.J. Shaw, Phys. Earth. Planet. Inter. 124 (2001) 71.
[30] I. Efthimiopoulos, C. Buchan, Y.J. Wang, Sci. Rep. 6 (2016) 24246.
[31] I. Efthimiopoulos, J.M. Zhang, M. Kucway, C.Y. Park, R.C. Ewing, Y.J. Wang, Sci. Rep. 3 (2013) 2665.
[32] J.G. Zhao, H.Z. Liu, L. Ehm, Z.Q. Chen, S. Sinogeikin, Y.S. Zhao, G.D. Gu, Inorg. Chem. 50 (2011) 11291.
[33] Y.M. Ma, G.T. Liu, P.W. Zhu, H. Wang, X. Wang, Q.L. Cui, J. Liu, Y.M. Ma, J. Phys. Condens. Matter 24 (2012) 475403.
[34] J.G. Zhao, H.Z. Liu, L. Ehm, D.W. Dong, Z.Q. Chen, G.D. Gu, J. Phys. Condens. Matter 25 (2013) 125602.
[35] Z.H. Yu, L. Wang, Q.Y. Hu, J.G. Zhao, S. Yan, K. Yang, S. Sinogeikin, G.D. Gu, H.K. Mao, Sci. Rep. 5 (2015) 15939.
[36] R. Vilaplana, D. Santamaría-Pérez, O. Gomis, F.J. Manjón, J. González, A. Segura, A. Muñoz, P. Rodríguez-Hernández, E. Pérez-González, V. Marín-Borrás, V. Muñoz-Sanjose, C. Drasar, V. Kucek, Phys. Rev. B 84 (2011) 184110.
[37] A. Polian, M. Gauthier, S.M. Souza, D.M. Trichês, J.C. de Lima, T.A. Grandi, Phys. Rev. B 83 (2011) 113106.
[38] A. Nakayama, M. Einaga, Y. Tanabe, S. Nakano, F. Ishikawa, Y. Yamada, High. Press. Res. 29 (2009) 245.
[39] B.X. Chen, C. Uher, L. Iordanidis, M.G. Kanatzidis, Chem. Mater. 9 (1997) 1655.
[40] A. Cantarero, J. Martinez-Pastor, A. Segura, A. Chevy, Phys. Rev. B 35 (1987) 9586.
[41] H. Mizoguchi, H. Hosono, N. Ueda, H. Kawazoe, J. Appl. Phys. 78 (1995) 1376.
[42] M. Schoijet, Sol. Ener. Mater 1 (1979) 43.
[43] J.G. Zhao, L.X. Yang, Z.H. Yu, Y. Wang, C.Y. Li, K. Yang, Z.G. Liu, Y. Wang, Inorg. Chem. 55 (2016) 3907.
[44] J.M. Besson, J. Cernogora, R. Zallen, Phys. Rev. B 22 (1980) 3866.
[45] V.V. Struzhkin, A.F. Goncharov, R. Caracas, H.K. Mao, R.J. Hemley, Phys. Rev. B 77 (2008) 165133.
[46] Y.A. Sorb, V. Rajaji, P.S. Malavi, U. Subbarao, P. Halappa, S.C. Peter, S. Karmakar, C. Narayana, J. Phys. Condens. Matter 28 (2016) 015602.
[47] P.P. Kong, F. Sun, L.Y. Xing, J. Zhu, S.J. Zhang, W.M. Li, Q.Q. Liu, X.C. Wang, S.M. Feng, X.H. Yu, J.L. Zhu, R.C. Yu, W.G. Yang, G.Y. Shen, Y.S. Zhao, R. Ahuja, H.K. Mao, C.Q. Jin, Sci. Rep. 4 (2014) 6679.
[48] J. Zhu, J.L. Zhang, P.P. Kong, S.J. Zhang, X.H. Yu, J.L. Zhu, Q.Q. Liu, X. Li, R.C. Yu, R. Ahuja, W.G. Yang, G.Y. Shen, H.K. Mao, H.M. Weng, X. Dai, Z. Fang, Y.S. Zhao, C.Q. Jin, Sci. Rep. 3 (2013) 2016.
[49] C. Zhang, L.L. Sun, Z.Y. Chen, X.J. Zhou, Q. Wu, W. Yi, J. Guo, X.L. Dong, Z.X. Zhao, Phys. Rev. B 83 (2011), 140504(R).